(Received 12 February 2026, Accepted 26 March 2026, Scheduled 14 April 2026)

A Dual-Band Shared-Aperture Antenna Employing a Meshed Patch and AMC-Backed Fabry-Pérot Cavity

Chaoyuan Guo, Zhihan Liu, and Yufeng Liu*

School of Physics and Electronic Engineering, Shanxi University, Taiyuan 030006, China

ABSTRACT: A low-profile, dual-band, shared-aperture antenna with a large frequency ratio is presented, based on a meshed patch and an AMC-backed Fabry-Pérot (F-P) cavity. By taking advantage of the weak frequency sensitivity of grid slotting in meshed patches, the upper meshed patch is utilized as both the parasitic patch for the low-frequency antenna and the partially reflective surface (PRS) for the high-frequency F-P cavity, thereby simplifying the overall structure. Meanwhile, the AMC ground is employed to control the reflection phase and reduce the cavity height to $\lambda/4$, which enables both antennas to share the same aperture within an 8-mm profile. A prototype is fabricated and tested at 1.6 GHz and 15.14–15.46 GHz. Measured results demonstrate a frequency ratio of 1:9.6, a peak gain of 6.2 dBi at 1.6 GHz, a peak gain of 11.8 dBi in the high-frequency band, and a port isolation better than 17 dB. The proposed antenna features compact size, low profile, and efficient structural reuse, making it attractive for integrated multi-band communication systems.

1. INTRODUCTION

With the rapid development of 5G communication, unmanned aerial vehicles (UAVs), and aerospace technologies, multi-band and highly integrated antennas have become a core requirement for communication systems [1, 2]. Traditional multi-antenna configurations suffer from problems such as large space occupation, severe electromagnetic interference, and high system costs [3]. Shared-aperture technology, which enables multi-band antennas to share a single radiation aperture, has emerged as a key technical solution to these issues [4].

Fabry-Pérot (F-P) cavity antennas have attracted significant attention in shared-aperture design because of their simple feeding structure, high gain, and low manufacturing cost [5–7]. Current research on F-P resonant cavity-based shared-aperture antennas mainly focuses on narrow frequency ratio scenarios. For example, the dual-frequency shared-aperture antenna proposed in [8] has a frequency ratio of only 1:1.8, which does not satisfy the requirements of wideband communication; the design in [9] adopts a two-layer partially reflective surface (PRS) structure to achieve dual-frequency operation; however, it has high processing complexity and a large profile height ($\lambda/2$); the PRS unit design in [10] by cutting periodic grooves on microstrip patches improves aperture utilization; however, the frequency ratio is only 1:11.7 with a low-frequency gain of less than 5 dBi. Meshed patch antennas achieve a lightweight design through hollow grid structures, and grid slotting has a negligible impact on the operating frequency [11, 12], providing the possibility of reusing the PRS structure of the F-P resonant cavity. However, existing studies have not fully utilized this characteristic to realize large frequency ratio shared-aperture designs [13, 16].

This study proposes a dual-frequency shared-aperture antenna design with a large frequency ratio, featuring three core innovations: (1) Leveraging the minimal frequency impact of grid slotting in meshed patches, the top layer is reused to serve both as the parasitic layer of the meshed patch and the PRS of the F-P resonant cavity, eliminating the need for an additional PRS structure and simplifying the antenna design; (2) Replacing the traditional metal ground plane with an artificial magnetic conductor (AMC) structure reduces the height of the F-P resonant cavity from $\lambda/2$ to $\lambda/4$ (8 mm), unifying it with the operating height of the meshed patch antenna to achieve complete aperture sharing and significantly reduce the antenna profile; (3) Adopting orthogonal polarization design (y-polarization for the meshed patch and x-polarization for the F-P resonant cavity) ensures better port isolation of better than -17 dB, effectively suppressing inter-port mutual coupling. The measured results verify the excellent performance of the design in the 1.6 GHz and 15.14–15.46 GHz bands with a frequency ratio of 1:9.6, providing a new solution for wideband shared-aperture antenna design.

2. DESIGN METHOD OF THE DUAL-FREQUENCY SHARED-APERTURE ANTENNA

2.1. Antenna Structure

The antenna adopts an overall double-layer dielectric substrate structure, as shown in Fig. 1. The bottom dielectric substrate (F4B, $\varepsilon_r = 2.65$, thickness 1.6 mm) is printed with a double-layer meshed patch, where the bottom-meshed patch serves as the main radiator, and the top-meshed patch functions as both a parasitic layer and the PRS of the F-P resonant cavity. The unit structure of the bottom-meshed patch is designed as an AMC to adjust the reflection phase. The air gap height between the

* Corresponding author: Yufeng Liu (liuyufeng@sxu.edu.cn).

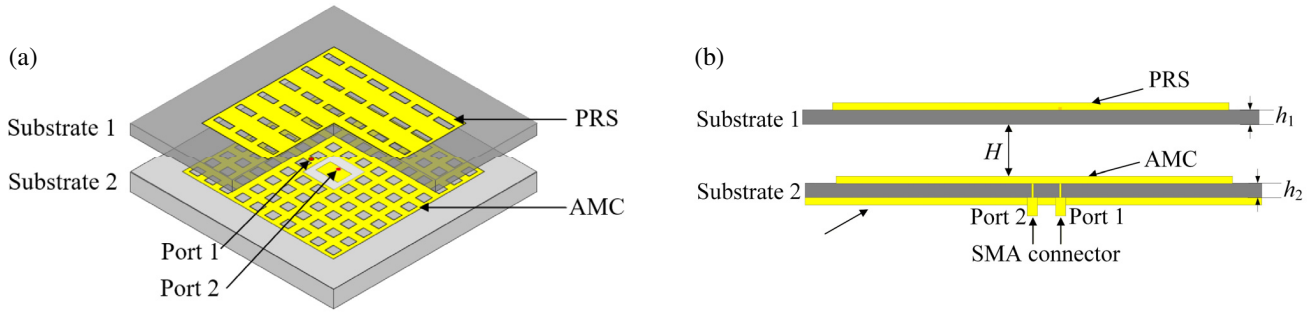

FIGURE 1. Schematic of shared-aperture antenna. (a) 3D diagram. (b) Side view.

two dielectric substrates is fixed at 8 mm to unify the operating height of the dual-frequency antenna. The feed source of the F-P resonant cavity is a 15.5 GHz microstrip patch antenna, which is orthogonally polarized to the meshed patch antenna to reduce mutual coupling.

The core design idea is to reduce the number of antenna layers through structure reuse and to adjust the profile of the F-P resonant cavity using the AMC structure, thereby achieving aperture sharing and performance optimization of the dual-frequency antenna. The specific process is as follows: first, a double-layer meshed patch antenna was designed, and the impact of grid slotting on the frequency was verified to lay the foundation for structure reuse; second, the top-meshed patch was reused as the PRS of the F-P resonant cavity to complete the preliminary design of the F-P resonant cavity; finally, the height of the resonant cavity was adjusted through the AMC structure to realize height unification and aperture sharing of the dual-frequency antenna.

2.2. Design of the Double-Layer Meshed Patch Antenna

The meshed patch antenna adopts coaxial feeding. The bottom patch has a size of 55 mm × 55 mm, with a 10×10 periodic slot design (slot length $a_1 = 3$ mm, slot width $b_1 = 3$ mm, period $p_1 = 5.5$ mm), and the top parasitic patch has a size of 48 mm × 48 mm, with a 6×6 periodic slot design (slot length $a_2 = 4$ mm, slot width $b_2 = 4$ mm, period $p_2 = 8$ mm), as shown in Fig. 2. The dielectric substrate is F4B material ($\varepsilon_r = 2.65$, loss tangent $\tan\delta = 0.001$), with a bottom substrate thickness $h_1 = 1.6$ mm and a top substrate thickness $h_2 = 0.8$ mm. The air gap height H between the two substrates is 8 mm.

The influence of slot size on the reflection coefficient was analyzed through simulations to verify the feasibility of structure reuse. As shown in Figs. 2(b) and (c), when the slot length a_2 increased from 2.8 to 3.2 mm, the resonant frequency offset of the double-layer meshed patch antenna was 0.04 and 0.01 GHz, respectively (2.5% impact, respectively); and when the slot width b_2 increased from 2.8 to 3.2 mm, the resonant frequency offset was less than 0.01 GHz (less than 0.6% impact). These results consistently demonstrate that the impact of grid slotting on the operating frequency of the meshed patch antenna is less than 3%, providing key theoretical support for reusing the top layer as the PRS of the F-P resonant cavity.

After adding the top parasitic patch, the impedance bandwidth can be effectively broadened through the coupling effect between the two metal layers. As shown in Fig. 3(a), the −10 dB impedance bandwidth of the single-layer meshed patch antenna is only 20 MHz (1.61–1.63 GHz). With the addition of the top parasitic patch, the 10 dB impedance bandwidth was expanded to 30 MHz (1.59–1.62 GHz), and the relative bandwidth increased from 1.2% to 1.9% (50% bandwidth improvement). Fig. 3(b) shows the 3D radiation pattern of the double-layer meshed patch antenna at 1.6 GHz, with a simulated gain of 7.57 dBi. The half-power beamwidths (HPBWs) of the E-plane and H-plane are 82° and 86°, respectively, exhibiting good omnidirectional radiation characteristics to meet low-frequency communication needs.

2.3. Design of the F-P Resonant Cavity

The PRS unit of the F-P resonant cavity directly reuses the top-meshed patch structure with a period $P_{\mathrm{PRS}} = 8$ mm, which is consistent with the slot period of the top parasitic patch, as shown in Fig. 4(a). For the simulation analysis of the PRS unit, its simulation model is presented in Fig. 4(b). The reflection performance of the unit in the x-polarization direction is analyzed via the Computer Simulation Technology (CST) simulation software, and the corresponding reflection amplitude and phase curves are depicted in Fig. 4. The square annular metal structure of the PRS unit is printed on the top dielectric substrate (F4B, thickness = 0.8 mm), and the core design goal is to optimize its size to meet the reflection characteristic requirements at the operating frequency of the F-P resonant cavity (15.5 GHz).

To verify the operating mode of the antenna, the electric field distribution characteristics at the low band of 1.6 GHz and high band of 15.5 GHz are obtained by simulation: for the low band, the current is mainly concentrated in the metal grid area of the bottom-meshed patch, and the top parasitic patch forms a coupling current. Radiation is realized through the current coupling of the two patches, which is consistent with the operating mode of the parasitic patch antenna. Electric field distribution nephogram of the antenna at 1.6 GHz as shown in Fig. 2(d). For the high band, the electric field is mainly concentrated in the 8 mm air gap area of the F-P resonant cavity, and a strong electric field resonance is formed between the top PRS and bottom AMC. The electromagnetic energy is radiated outward through the PRS, which is consistent with the resonant radiation mode of the F-P cavity antenna. Electric field distribution nephogram of the antenna at 15.5 GHz as shown in Fig. 2(e).

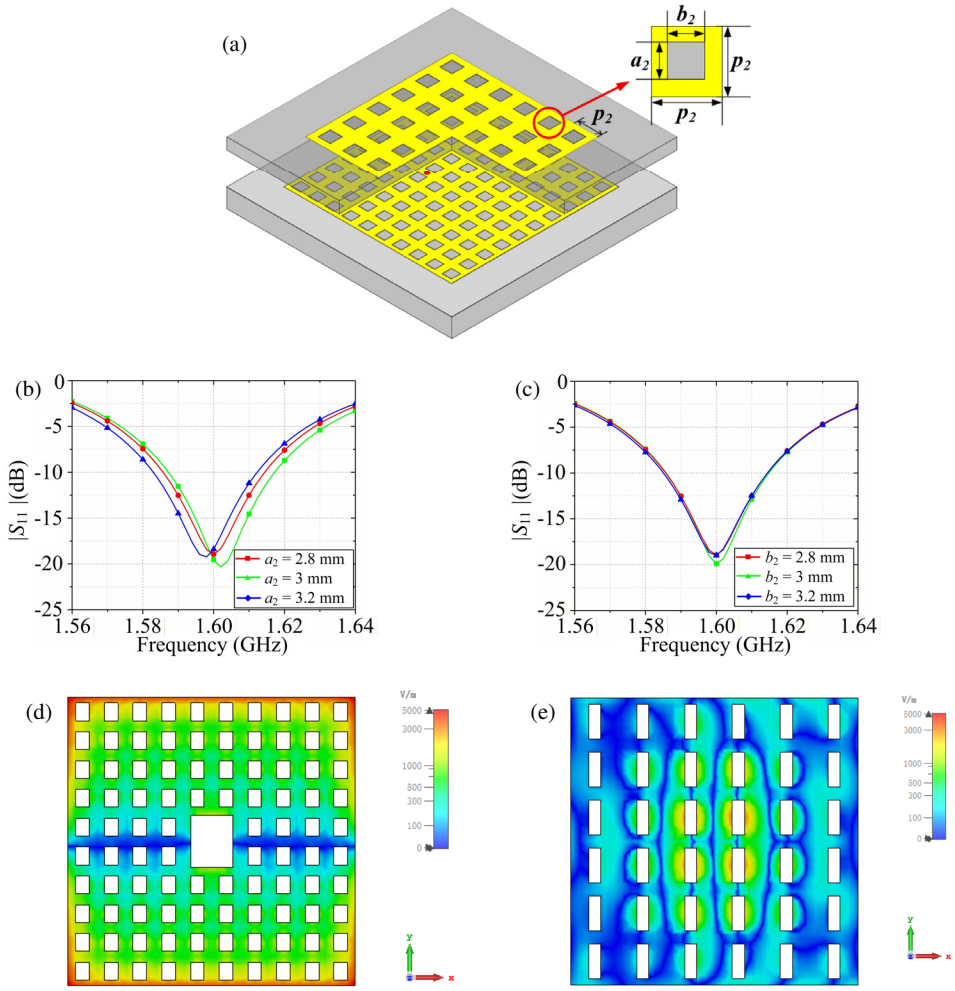

FIGURE 2. Effect of different slot sizes on reflection coefficient. (a) Schematic diagram of structural dimensions for the dual-layer meshed patch antenna. (b) Influence of different slot lengths on a double-layer meshed patch. (c) Influence of different slot widths on a double-layer meshed patch. The distribution of (d) high-frequency and (e) low-frequency electric fields.

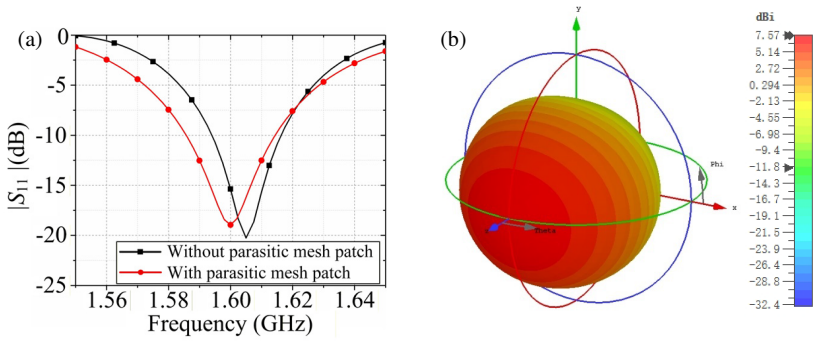

FIGURE 3. Simulation results of double-layer meshed patch antenna performance. (a) Effect of the presence or absence of parasitic patches on the reflection coefficient. (b) Radiation pattern at 1.6 GHz.

The simulation results show that the reflection phase of the PRS unit has good adjustability with changes in size: as shown in Fig. 4(c), when L_{PRS} increases from 1.6 mm to 2.4 mm, the reflection phase at 15.5 GHz decreases from 135° to 92° with an adjustment range of 43°; Fig. 4(d) indicates that when WPRS increases from 5.4 mm to 6.2 mm, the reflection phase decreases from 128° to 85° with the same adjustment range of 43°. In contrast, the reflection amplitude of the PRS unit changes slightly with size, stabilizing between 0.81 and 0.85 at 15.5 GHz (as shown in Figs. 4(e) and (f)), which satisfies the requirement of the F-P resonant cavity for the PRS reflection amplitude (0.7–0.9). The finally determined PRS unit has a reflection amplitude of 0.83 and a reflection phase of 113° at

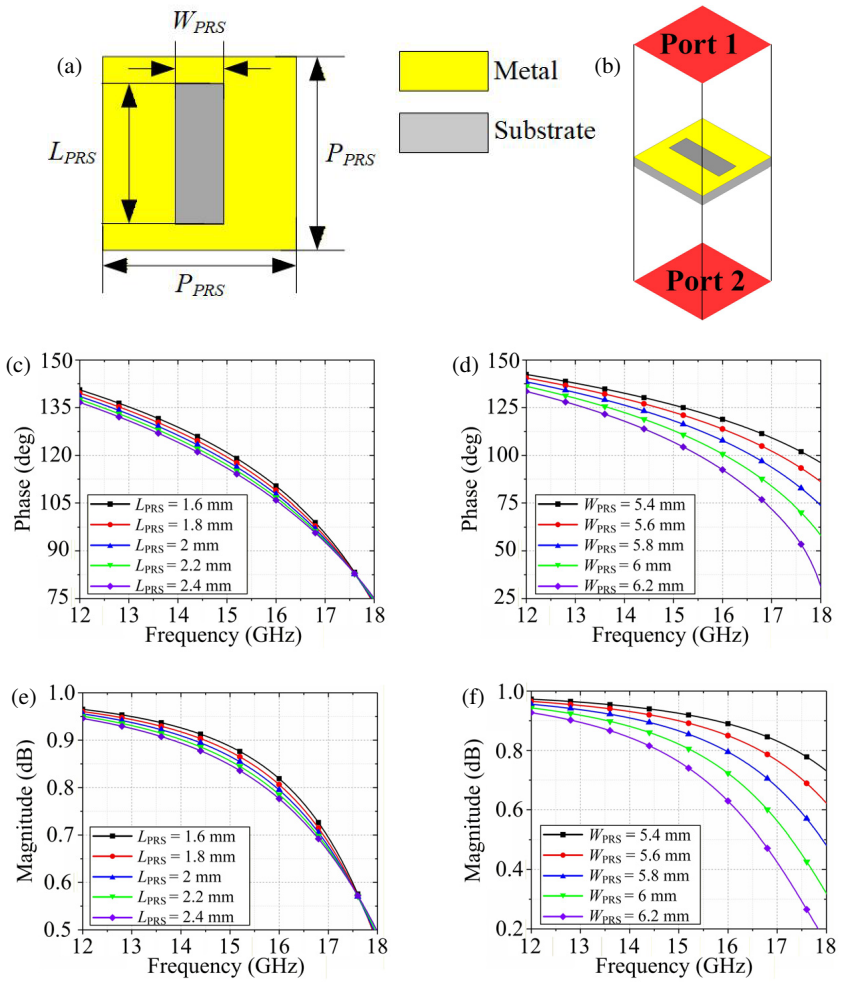

FIGURE 4. Design and reflection characteristics of PRS unit for the F-P resonant cavity. (a) PRS unit structure. (b) PRS unit port setting. (c) Reflection phase with different LPRS. (d) Reflection phase with different WPRS. (e) Reflection amplitude with different LPRS. (f) Reflection amplitude with different WPRS.

15.5 GHz, ensuring the high-gain performance of the F-P resonant cavity.

According to the phase-matching condition of the F-P resonant cavity [16]:

$$\varphi_{\text{PRS}} - \varphi_{\text{GP}} - \frac{4\pi}{\lambda}h = 2N\pi \tag{1}$$

where φ_{PRS} is the reflection phase of the PRS unit, φ_{GP} the reflection phase of the metal ground plane, λ the operating wavelength, and N an integer. Substituting $\varphi_{\text{PRS}} = 113°$, $\varphi_{\text{GP}} = 180°$, $\lambda = 19.35$ mm (corresponding to 15.5 GHz), and $N = 0$, the preliminary design value of the resonant cavity height is 12.5 mm. The influence of the cavity height on the performance of the F-P resonant cavity was optimized through simulations. As shown in Fig. 5(a), when the cavity height $H = 13$ mm, the reflection coefficient of the F-P resonant cavity antenna at 15.5 GHz was the lowest (-18.7 dB) with optimal impedance matching. The 3D radiation pattern of the antenna at this height is shown in Fig. 5(b), with a simulated gain of 14.7 dBi. The HPBW of the E-plane and H-plane are 32° and 30°, respectively, exhibiting good directional radiation characteristics to satisfy high-frequency long-distance communication requirements.

The theoretical gain of the F-P resonant cavity antenna in this work is calculated according to the classic formula $G = 4\pi A/\lambda^2$, where the effective radiation aperture of the antenna $A = 74\,\text{mm} \times 74\,\text{mm}$, and the operating wavelength is corresponding to 15.5 GHz $\lambda = 19.35$ mm. The calculated theoretical gain is about 15.2 dBi, and the deviation (0.5 dBi) from the simulated gain of 14.7 dBi is mainly caused by dielectric substrate loss and metal ohmic loss.

The size of the low-frequency meshed patch determines the effective radiation aperture of the high-frequency F-P cavity. In this design, the aperture is $3.8\lambda \times 3.8\lambda$. Increasing the aperture can further improve the high-frequency gain but will increase the overall volume of the antenna synchronously. Therefore, the low-frequency antenna size is a volume constraint rather than a performance limitation on the high-frequency gain.

The core of the proposed design method is the structural reuse of the meshed patch and the phase control of AMC, which is applicable to the medium frequency ratio scenario of 1:3∼1:8. Dual-band aperture sharing can be achieved only by

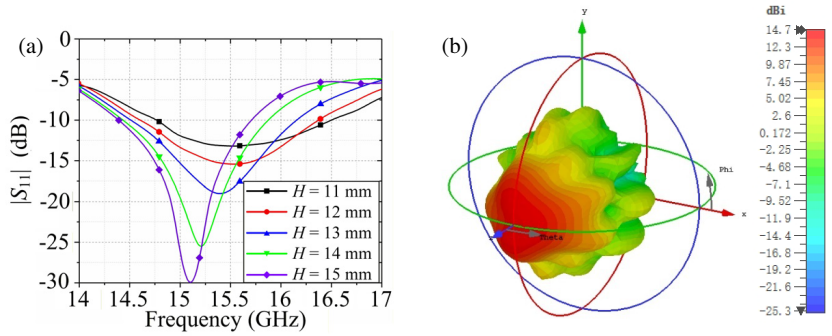

FIGURE 5. Design and performance of F-P resonant cavity antenna. (a) Effect of cavity height on reflection coefficient. (b) Radiation pattern at 15.5 GHz.

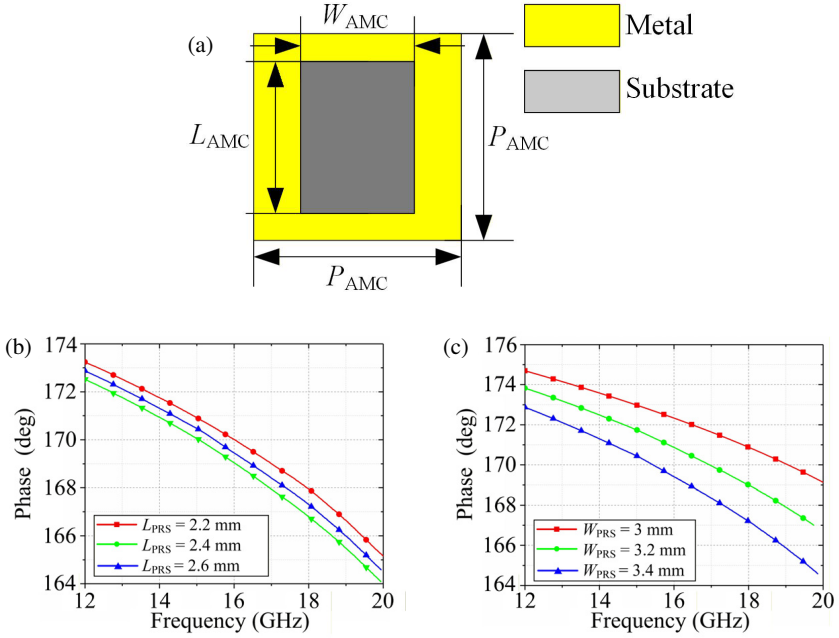

FIGURE 6. Design and reflection characteristics of AMC unit. (a) AMC unit structure. (b) Reflection phase with different LAMC. (c) Reflection phase with different WAMC.

optimizing the meshed patch period, AMC unit size, and F-P cavity height according to the specific medium frequency ratio, with no core technical limitations related to the frequency ratio.

2.4. AMC Structure Design and Aperture Sharing Implementation

To unify the height of the F-P resonant cavity with the meshed patch antenna (8 mm), an AMC structure is designed to replace the traditional metal ground plane, and the height of the resonant cavity is optimized by adjusting the reflection phase. In this case, the phase-matching condition is revised to

$$\varphi_{\text{PRS}} - \varphi_{\text{AMC}} - \frac{4\pi}{\lambda} h = 2N\pi \tag{2}$$

where φ_{AMC} is the reflection phase of the AMC structure and $h = 8$ mm. Substituting the known parameters, $\varphi_{\text{AMC}} \approx 169°$ is obtained, indicate that the AMC structure must achieve a reflection phase of 169° at 15.5 GHz.

The AMC unit adopts a square annular metal structure printed on the bottom dielectric substrate (F4B, thickness 1.6 mm), as shown in Fig. 6(a). The unit period $P_{\text{AMC}} = 5.5$ mm, consistent with the slot period of the bottom-meshed patch. The square annular aperture length LAMC and width W_{AMC} are key adjustment parameters. The simulation results show, in Fig. 6(b), that when the slot width W_{AMC} is fixed at 3 mm, and the slot length L_{AMC} increases from 2.2 mm to 2.6 mm, the reflection phase of the AMC unit at 15.5 GHz decreases from 172° to 165° with an adjustment range of 7°; Fig. 6(c) indicates that when the slot length L_{AMC} is fixed at 2.4 mm, and the slot width W_{AMC} increases from 3 mm to 3.4 mm, the reflection phase decreases from 170° to 163° with an adjustment range of 7°. Through joint optimization, the final parameters of the AMC unit were determined as $L_{\text{AMC}} = 3.2$ mm and $W_{\text{AMC}} = 2.4$ mm, achieving a reflection phase of 169° at 15.5 GHz, which fully satisfied the design target.

TABLE 1. Structural parameters of aperture-sharing antenna.

Parameter	P_{PRS}	L_{PRS}	W_{PRS}	P_{AMC}	L_{AMC}
Value (mm)	8	2	5.8	5.5	2.4
Parameter	W_{AMC}	H	h_1	h_2	
Value (mm)	3.2	8	1.6	0.8	

The overall structural parameters of the antenna are listed in Table 1. The top layer functions both as a parasitic patch and a PRS. The bottom layer functions both as a radiator and an AMC, with a structure reuse rate of 100%. No additional structural layers are required, thereby simplifying the antenna design. The operating mechanism of the dual-frequency antenna is as follows: In the low-frequency band (1.6 GHz), the bottom-meshed patch serves as the main radiator, and the top-meshed patch serves as a parasitic layer to achieve wideband radiation through coupling; in the high-frequency band (15.5 GHz), the top-meshed patch serves as the PRS, and the bottom AMC structure serves as a reflective surface, forming an F-P resonant cavity with the feed source to achieve high-gain directional radiation. Meanwhile, the meshed-patch antenna adopts y-direction polarization, and the F-P resonant cavity antenna adopts x-direction polarization. Orthogonal polarization further suppresses inter-port mutual coupling, thereby ensuring the independence of the dual-frequency operation.

3. RESULTS AND DISCUSSION

The antenna prototype was fabricated according to the design parameters, as shown in Figs. 7(a) and (b). Both dielectric substrates were made of F4B material with an aperture size of 74 mm × 74 mm, fixed by four nylon screws to ensure an air gap height of 8 mm between the two substrates. The thicknesses of the bottom and the top dielectric substrates were 1.6 mm, and 0.8 mm, respectively. The metal structure is fabricated using copper foil etching technology with an etching precision of ±0.05 mm, ensuring the consistency of the structural parameters. Four nylon screws (relative permittivity $\varepsilon_r \approx 3.0$, diameter 3 mm, height 8 mm) are used to fix the dual dielectric substrates in this prototype, and all screws are arranged in the outer area of the antenna's 74 mm × 74 mm radiation aperture. To verify their electromagnetic influence, the antenna performance of two models (with/without nylon screws) is compared by simulation. The results show that the nylon screws have almost no effect on the antenna's resonant frequency and gain, and the change in the sidelobe level of the radiation pattern is less than 0.1 dB, indicating that their electromagnetic influence is negligible.

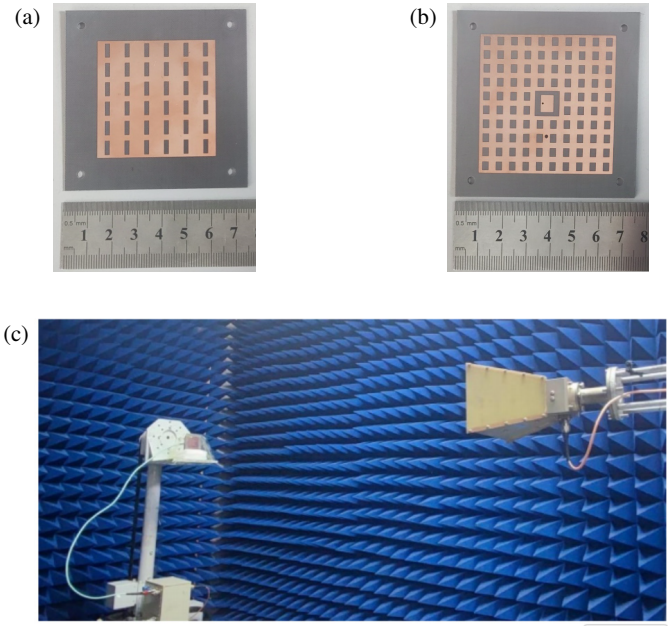

FIGURE 7. Fabricated prototype and measurement environment of shared-aperture antenna. (a) Top view of the antenna. (b) Bottom view of the antenna. (c) Schematic of measurement environment.

The measurement equipment comprised an Agilent E8363B vector network analyzer (frequency range: 10 MHz–40 GHz) and an anechoic chamber (size: 5 m × 5 m × 3 m). A vector network analyzer was used to measure the reflection coefficients ($|S_{11}|$, $|S_{22}|$) and isolation ($|S_{12}|$) of the antenna, and the far-field measurement method was adopted in the anechoic chamber to measure the gain and radiation pattern of the antenna. The measurement environment is shown in Fig. 7(c) to ensure the accuracy of the measurement results.

The measurement results of the reflection coefficient and isolation, as shown in Fig. 8(a), indicate that the measured −10 dB impedance bandwidth of the high-frequency band (F-P resonant cavity antenna) is 15.14–15.46 GHz (320 MHz), which is consistent with the simulation result (15.0–15.5 GHz) with a relative bandwidth of 2.1%, meeting the bandwidth requirements of high-frequency communication; the measured resonant frequency of the low-frequency band (double-layer meshed patch antenna) is 1.6 GHz; however, the −10 dB impedance bandwidth does not meet the design requirement. This is because the thickness deviation of the dielectric substrate (±0.1 mm) leads to insufficient consistency of the air gap height, thereby affecting impedance matching.

To quantify the influence of manufacturing errors on the low-band impedance matching, simulation analyses of three core errors in the antenna processing are carried out: (1) Dielectric substrate thickness deviation: When the thickness of the F4B substrate deviates from the design value by ±0.1 mm, the antenna resonant frequency shifts by 0.02∼0.03 GHz, and the real part of the input impedance deviates by 15∼20 Ω; (2) Air gap height deviation: When the air gap height deviates from 8 mm by ±0.2 mm, the coupling coefficient of the dual-layer patch decreases by 10%∼15%, and the −10 dB impedance bandwidth narrows by 5∼8 MHz; (3) Metal etching precision deviation: When the etching size deviates by ±0.05 mm, the effective radiation area of the meshed patch changes by 3%∼5%, and the reflection coefficient $|S_{11}|$ deteriorates by 3∼5 dB. The superposition of the above processing errors is the core reason for the low-band impedance bandwidth failing to meet the design requirement, among which the dielectric substrate thickness deviation is the main inducing factor.

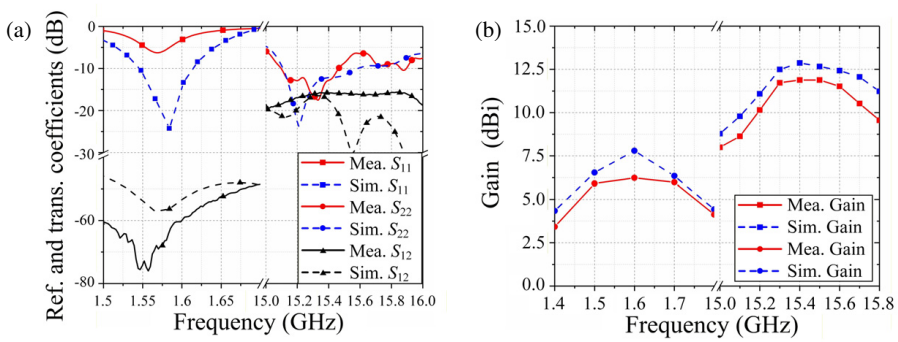

FIGURE 8. Comparison of the reflection coefficient and gain of shared-aperture antenna. (a) Simulation and measurement reflection performance comparison. (b) Maximum gain curve comparison of simulation and measurement.

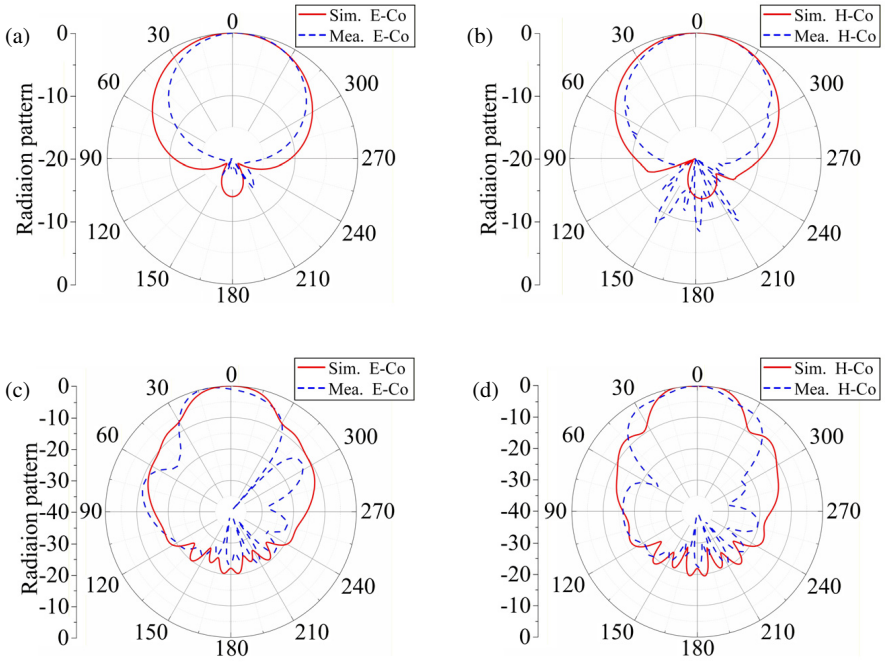

FIGURE 9. Comparison of radiation patterns at different frequencies. (a) E-plane at 1.6 GHz. (b) H-plane at 1.6 GHz. (c) E-plane at 15.4 GHz. (d) H-plane at 15.4 GHz.

In terms of isolation, the port isolation is less than -30 dB in the low-frequency band (1.6 GHz) and less than -17 dB in the high-frequency band (15.14–15.46 GHz), both meeting the isolation requirements of shared-aperture antennas (usually less than -15 dB). This is mainly due to the orthogonal polarization design and the isolation effect of the AMC structure, which effectively suppresses the electromagnetic coupling between the two frequency bands.

The gain measurement results indicate that, as shown in Fig. 8(b), the measured peak gain of the double-layer meshed patch antenna at 1.6 GHz is 6.2 dBi, compared with the simulated gain of 6.9 dBi, with a measurement deviation of 0.7 dBi; the measured peak gain of the F-P resonant cavity antenna at 15.4 GHz is 11.8 dBi, compared with the simulated gain of 12.9 dBi, with a measurement deviation of 1.1 dBi. Which corresponding to 21.3% and 8.35% aperture efficiency at 1.6 GHz and 15.4 GHz, respectively. The main reasons for the gain attenuation include the ohmic loss of the metal structure, dielectric loss of the substrate, structural parameter deviations caused by manufacturing errors, and electromagnetic interference in the measurement environment.

Regarding the slight deviation between the measured and simulated results, a systematic analysis and verification from the perspectives of testing and fabrication have been carried out in this paper, and the causes of the deviation are mainly objective factors in engineering implementation. First, the weak electromagnetic background clutter in the anechoic chamber during the test has a slight impact on the accurate measurement of the sidelobe level of the radiation pattern in the high-frequency band. Second, a parallelism deviation of ± 0.1 mm exists in the dual dielectric substrates during manual assembly, which affects the height uniformity of the 8 mm air gap and further leads to minor deviations in impedance matching and radiation characteristics. Third, the batch difference of dielec-

TABLE 2. Comparison of performance between this antenna and reference antennas.

Ref.	Freq. (GHz)	Bandwidth	Aperture Efficiency (%)	Freq. ratio	Gain (dBi)	Feed Network	Isolation (dB)	Antenna Type
[8]	5.3; 9.6	5.2 to 5.45 GHz; 9.4 to 10.1 GHz	62; 55.6	1:1.8	16.0; 20.0	Yes	35; 40	F-P; F-P
[9]	3.45; 5	3.4 to 3.47 GHz; 4.94 to 5.05 GHz	77; 74	1:1.4	13.7; 16.8	No	32.6; 41.2	F-P; F-P
[14]	11; 17	10.5 to 11.6 GHz; 16.5 to 17.6 GHz	26.4; 20	1:1.5	21.3; 23.8	No	Not reported	FRA; FTA
[15]	1.6; 12.5	1.52 to 1.69 GHz; 11.35 to 13.15 GHz	Not reported	1:7.6	3.2; 5.0	Yes	35; 30	Slot antenna; DRA
[16]	3.5; 28	3.41 to 3.59 GHz; 26.62 to 30.26 GHz	12.8	1:8	12.79; 8.75	Yes	35; 30	PRS; Patch
This work	1.6; 15.5	1.6 GHz; 15.14 to 15.46 GHz	21.3; 10.5	1:9.6	6.99; 12.8	No	30; 17	F-P; Mesh Patch Antenna

FRA: Folded Reflectarray Antenna; FTA: Folded Transmitarray Antenna; DRA: Dielectric Resonator Antenna.

tric substrates causes slight fluctuations in the loss tangent of F4B, resulting in the measured attenuation of antenna gain.

To verify the validity of the measured data, the test system was accurately calibrated with short-open-load-through (SOLT) full two-port calibration using the Agilent 85052D calibration kit, and the core structural parameters of the prototype were remeasured for multiple times. It is confirmed that the deviation between the processed dimensions and the design values is controlled within the engineering allowable range of ± 0.05 mm. The results after calibration and remeasurement show that the deviation between the measured and simulated results is within a reasonable engineering range: the deviation of the reflection coefficient $|S_{11}|$ is less than 0.5 dB in the low-frequency band and less than 1.0 dB in the high-frequency band; the deviation of the half-power beamwidth (HPBW) of the radiation pattern is less than 3°, and the deviation of the sidelobe level is less than 1 dB. All core electromagnetic performance indicators of the antenna meet the design expectations, and the deviation has no impact on the practical application performance of the antenna.

The radiation pattern measurement results show that as shown in Fig. 9, at 1.6 GHz (low-frequency band), the measured HPBW of the E-plane is 85°, and that of the H-plane is 88°, which are basically consistent with the simulation results (E-plane: 82°, H-plane: 86°), with sidelobe levels lower than -15 dB and -9 dB, respectively; at 15.4 GHz (high-frequency band), the measured HPBW of the E-plane is 34°, and that of the H-plane is 32°, which are in good agreement with the simulation results (E-plane: 32°, H-plane: 30°), with sidelobe levels lower than -10.6 dB and -8.6 dB, respectively. The difference between the measured and simulated radiation patterns in the high-frequency band is slightly larger, mainly owing to more significant positioning errors and external electromagnetic interference during manual measurement in the high-frequency band; however, the overall directional radiation characteristics are maintained.

The performance of the proposed antenna was compared with that of recently reported shared-aperture antennas in the literature, and the results are listed in Table 2. Compared with [8], the proposed antenna has a significantly higher frequency ratio (1:9.6 vs. 1:1.8) and does not require a complex feeding network; compared with [9], the profile height of the proposed antenna (8 mm) is only half of that in [9], with a simpler structure; compared with [14], the proposed antenna has a higher low-frequency gain (6.2 dBi) and a larger frequency ratio. Overall, the proposed antenna has obvious advantages in the frequency ratio, structural complexity, profile thickness, and port isolation, making it more suitable for multi-band and miniaturized communication system applications. Additionally, compared with [15] and [16], the proposed antenna achieves a higher frequency ratio (1:9.6 vs. 1:7.6 and 1:8) and avoids complex feeding networks, demonstrating clearer advantages for multi-band miniaturized systems.

4. CONCLUSION

This study presents a dual-frequency shared-aperture antenna based on a Fabry-Pérot resonant cavity and a meshed patch. By employing structure reuse and AMC phase control techniques, the antenna achieves dual-frequency operation at 1.6 and 15.14–15.46 GHz with a frequency ratio of 1:9.6. The grid slotting effect on the resonant frequency was verified to be less than 3%, which enabled the top layer to serve as both a parasitic patch and a PRS, thereby simplifying the configuration. The AMC structure reduces the cavity height from $\lambda/2$ to $\lambda/4$ (8 mm), realizing a fully shared aperture and enhanced port isolation. The measured results demonstrate good performance: a peak gain of 6.2 dBi in the low band, a -10 dB impedance bandwidth of 320 MHz and a peak gain of 11.8 dBi at the high band, as well as port isolation better than -17 dB. Featuring a simple structure, low cost, and high integration, the proposed antenna is suitable for space- and weight-constrained multi-band systems such as UAVs and satellite communications.

The dual-band shared-aperture antenna proposed in this paper exhibits limited bandwidth owing to structural reuse constraints, with a relative bandwidth of 1.9% at 1.6 GHz and 2.1% at 15.14–15.46 GHz. To improve the bandwidth, several effective strategies are presented: using a tapered periodic grid patch or arc-shaped parasitic stubs for the lower band can extend the relative bandwidth beyond 5%, while a multi-parameter composite PRS array can increase that of the higher band to 4%–5%. Moreover, employing a low-loss polytetrafluoroethylene (PTFE) composite substrate can reduce impedance mismatch and bandwidth deterioration. The proposed methods can provide a valuable reference for the wideband design of similar dual-band shared-aperture antennas.

REFERENCES

[1] Zhang, J.-E., G. Liu, W.-W. Yang, and J.-X. Chen, "A tri-frequency shared-aperture antenna for cooperative work of V2X and millimeter-wave bands," *IEEE Antennas and Wireless Propagation Letters*, Vol. 24, No. 3, 776–780, Mar. 2025.

[2] Serup, D. E., G. F. Pedersen, and S. Zhang, "Dual-band shared aperture reflectarray and patch antenna array for S- and Ka-bands," *IEEE Transactions on Antennas and Propagation*, Vol. 70, No. 3, 2340–2345, Mar. 2022.

[3] Mei, P., S. Zhang, and G. F. Pedersen, "A dual-polarized and high-gain X-/Ka-band shared-aperture antenna with high aperture reuse efficiency," *IEEE Transactions on Antennas and Propagation*, Vol. 69, No. 3, 1334–1344, Mar. 2021.

[4] Ji, S., Y. Dong, S. Wen, and Y. Fan, "C/X dual-band circularly polarized shared-aperture antenna," *IEEE Antennas and Wireless Propagation Letters*, Vol. 20, No. 12, 2334–2338, Dec. 2021.

[5] Trentini, G. V., "Partially reflecting sheet arrays," *IRE Transactions on Antennas and Propagation*, Vol. 4, No. 4, 666–671, Oct. 1956.

[6] Alexopoulos, N. and D. Jackson, "Fundamental superstrate (cover) effects on printed circuit antennas," *IEEE Transactions on Antennas and Propagation*, Vol. 32, No. 8, 807–816, Aug. 1984.

[7] Weily, A. R., L. Horvath, K. P. Esselle, B. C. Sanders, and T. S. Bird, "A planar resonator antenna based on a woodpile EBG material," *IEEE Transactions on Antennas and Propagation*, Vol. 53, No. 1, 216–223, Jan. 2005.

[8] Qin, F., S. S. Gao, Q. Luo, C.-X. Mao, C. Gu, G. Wei, J. Xu, J. Li, C. Wu, K. Zheng, and S. Zheng, "A simple low-cost shared-aperture dual-band dual-polarized high-gain antenna for synthetic aperture radars," *IEEE Transactions on Antennas and Propagation*, Vol. 64, No. 7, 2914–2922, Jul. 2016.

[9] Liu, Z.-G., R.-J. Yin, Z.-N. Ying, W.-B. Lu, and K.-C. Tseng, "Dual-band and shared-aperture Fabry-Perot cavity antenna," *IEEE Antennas and Wireless Propagation Letters*, Vol. 20, No. 9, 1686–1690, Sep. 2021.

[10] Zhu, J., Y. Yang, S. Liao, S. Li, and Q. Xue, "Dual-band aperture-shared Fabry-Perot cavity-integrated patch antenna for millimeter-wave/sub-6 GHz communication applications," *IEEE Antennas and Wireless Propagation Letters*, Vol. 21, No. 5, 868–872, May 2022.

[11] Clasen, G. and R. Langley, "Meshed patch antennas," *IEEE Transactions on Antennas and Propagation*, Vol. 52, No. 6, 1412–1416, Jun. 2004.

[12] Turpin, T. W. and R. Baktur, "Meshed patch antennas integrated on solar cells," *IEEE Antennas and Wireless Propagation Letters*, Vol. 8, 693–696, 2009.

[13] Sun, Y., Z. N. Chen, Y. Zhang, H. Chen, and T. S. P. See, "Sub-wavelength substrate-integrated Fabry-Pérot cavity antennas using artificial magnetic conductor," *IEEE Transactions on Antennas and Propagation*, Vol. 60, No. 1, 30–35, Jan. 2012.

[14] Zhu, J., Y. Yang, S. Liao, and Q. Xue, "Dual-band antenna hybridizing folded transmitarray and folded reflectarray," *IEEE Transactions on Antennas and Propagation*, Vol. 70, No. 4, 3070–3075, Apr. 2022.

[15] Tong, C., B. Yang, X. Huang, N. Yang, X. Liu, and K. W. Leung, "Compact shared-aperture slot/DR antenna with large frequency ratio," *IEEE Antennas and Wireless Propagation Letters*, Vol. 22, No. 5, 1119–1123, May 2023.

[16] Zou, J., Y. Zhao, X. Yang, L. Ge, and Y.-X. Sun, "Dual-band dual-polarized shared-aperture grid antenna with large frequency ratio," *IEEE Antennas and Wireless Propagation Letters*, Vol. 22, No. 7, 1513–1517, Jul. 2023.